

# Surface velocity and mass balance of Ice Streams D and E, West Antarctica

ROBERT BINDSCHADLER

*Code 971, NASA Goddard Space Flight Center, Greenbelt, Maryland 20771, U.S.A.*

PATRICIA VORNBERGER

*General Sciences Corporation, 6100 Chevy Chase Drive, Laurel, Maryland 20707-2929, U.S.A.*

DONALD BLANKENSHIP

*Institute for Geophysics, University of Texas, Austin, Texas 78759, U.S.A.*

TED SCAMBOS

*National Snow and Ice Data Center, CIRES, University of Colorado, Boulder, Colorado 80309-0449, U.S.A.*

ROBERT JACOBEL

*Physics Department, St. Olaf College, Northfield, Minnesota 55057, U.S.A.*

**ABSTRACT.** Over 75 000 surface-velocity measurements are extracted from sequential satellite imagery of Ice Streams D and E to reveal a complex pattern of flow not apparent from previous measurements. Horizontal and vertical strain rates, calculated from surface velocity, indicate that the bed experiences larger basal shear where the surface of these ice streams is rougher. Ten airborne-radar profiles and one surface-based radar profile of ice thickness make possible the calculation of mass balance for longitudinal sections of each ice stream. Improved data-collection methods increase data density, substantially reducing random errors in velocity. However, systematic errors continue to limit the ability of the flux-differencing technique used here to resolve local variations in mass balance. Nevertheless, significant local variations in mass balance are revealed, while, overall, Ice Streams D and E are in approximate equilibrium. An earlier estimate of the net mass balance for Ice Stream D is improved.

## INTRODUCTION

Ice streams are critical elements of the dynamics of the West Antarctic ice sheet. They are important because they are large, they move rapidly and they drain most of the snow that accumulates over this ice sheet. Their speed and thickness determine the rate at which this ice sheet releases its mass to the ocean. Their size and the prevalence of numerous crevasse fields across their surface (a by-product of their speed) make them difficult to study by traditional surface-based techniques. However, these same characteristics make them well suited to study by remote-sensing methods.

Using surface-feature tracking on sequential imagery, Bindschadler and Scambos (1991) showed that the surface velocity of Ice Stream E exhibited considerable spatial variation — even in the middle of the ice stream, well away from the shearing margins. Thus, calculations of mass flux that use sparse velocity data are susceptible to large errors. A dense velocity data set also opens up a new avenue by which the dynamics of ice streams can be

studied. This was illustrated by MacAyeal and others (1995), who calculated the pattern of basal shear stress on Ice Stream E and showed that it also exhibits high spatial variability. Similarly, ice thickness and accumulation rate exhibit high spatial variability and are not adequately represented with sparse data.

The lack of adequate high-resolution spatial coverage has hampered earlier studies of West Antarctic ice-sheet mass balance. Ice Stream B is a case where detailed measurements of velocity, thickness and accumulation rate were collected and analyzed to reveal not only a strong negative mass balance but a complex pattern of local mass balances along the ice stream (Shabtaie and others, 1988; Whillans and Bindschadler, 1988). Complexity on an even finer scale was apparent when more detailed data sets of the ice-stream mouth were analyzed (Bindschadler and others, 1993).

This paper focuses on Ice Streams D and E, two of the major ice streams feeding the Ross Ice Shelf (Fig. 1). Surface velocities over most of each ice stream are measured with unprecedented detail for such a large

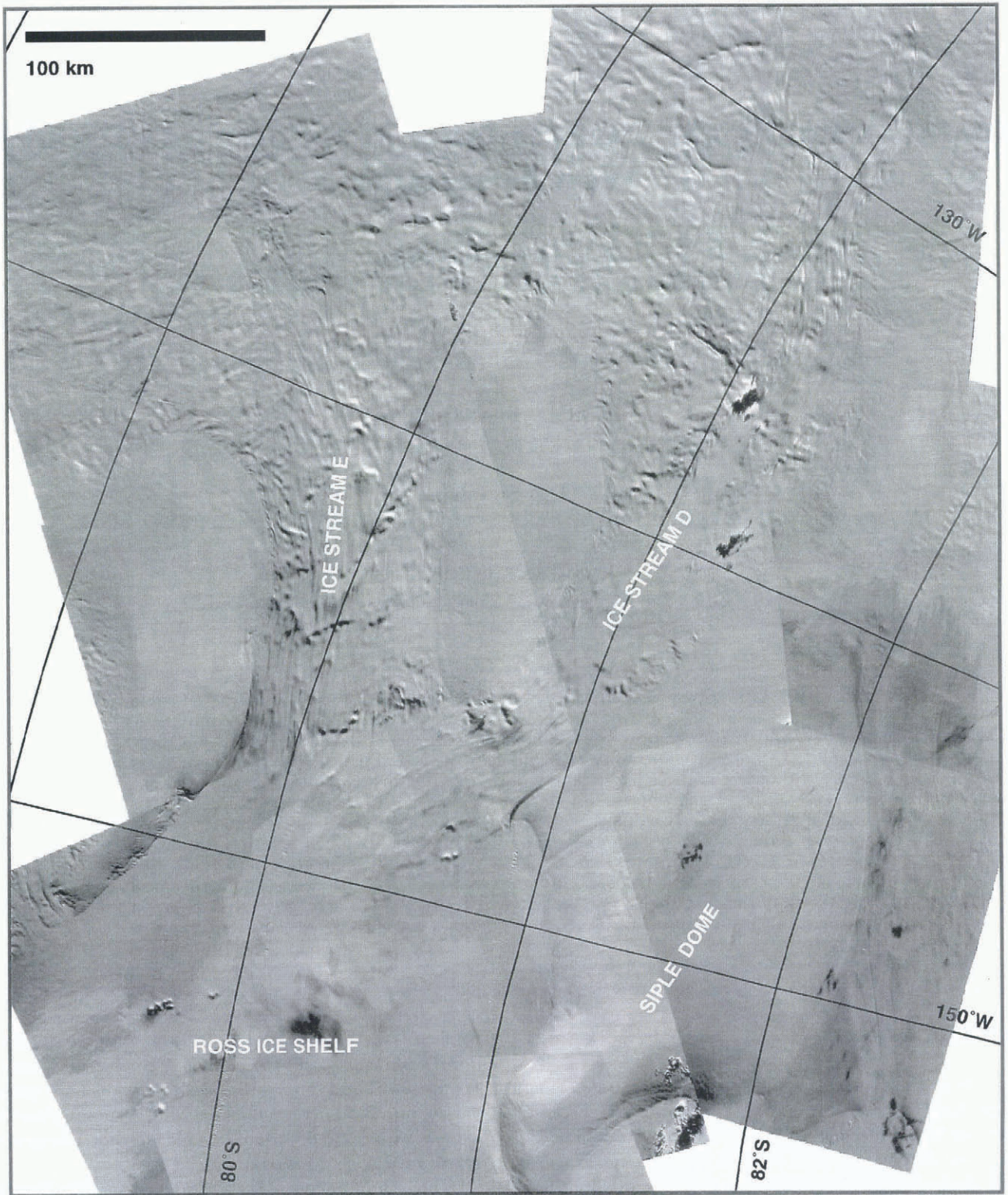


Fig. 1. Image mosaic of Ice Streams D and E using ten Landsat TM scenes. See Figure 2 for location of this region.

area. The pattern of surface velocity, interpreted in combination with the imagery showing surface undulations and numerous profiles of ice thickness measured by ice-penetrating radar, provides unique insights into the dynamic characteristics of these ice streams. Discharge fluxes across a number of ice-stream-wide transects (termed “gates” in this paper), including the discharge across the grounding lines, are calculated. These fluxes are used to determine the present pattern of mass balance on Ice Streams D and E, and substantially revise a

previous estimate of Ice Stream D’s discharge and mass balance (Shabtaie and Bentley, 1987).

#### DATA

A variety of methods was used to collect the data used in this paper. Sixteen Landsat Thematic Mapper (TM) images were used to determine surface velocities. These same images have been used previously to map a variety

of surface features of the ice streams and their catchment basins (Scambos and Bindschadler, 1991). Many of these same images were also used in the production of image maps (Ferrigno and others, 1994). Ice thickness was measured by an airborne ice-penetrating radar along ten transects and, near the grounding line, using a surface-based radar. Detailed surface-elevation, gravity and magnetic profiles were also measured from the aircraft but are not discussed here. Finally, surface-accumulation measurements were made by analyzing ten 20 m deep cores drilled from the surface. Each data set is described in more detail below.

**Surface velocity**

The method described by Scambos and others (1992) was used to derive surface velocities from the sequential, high-resolution satellite imagery of the ice streams. Briefly, each image is split into long-wavelength and short-wavelength images using digital filters. In each case, a filter cut-off wavelength of approximately 1 km was used. The long-wavelength images are then used to co-register each image pair. Using this co-registration, the short-wavelength images are used to track the motion of small, sharp features by cross-correlating their brightness patterns in each image (Scambos and others, 1992). Generally, we used a 16 pixel × 16 pixel area (roughly 450 m on a side, given the 28.5 m dimension of a TM pixel) or a 32 pixel × 32 pixel area to define the brightness pattern of any feature. The automated cross-correlation scheme determines the displacement of features to sub-pixel resolution as well as an index of the displacement uncertainty.

Figure 2 shows the location of the image pairs and

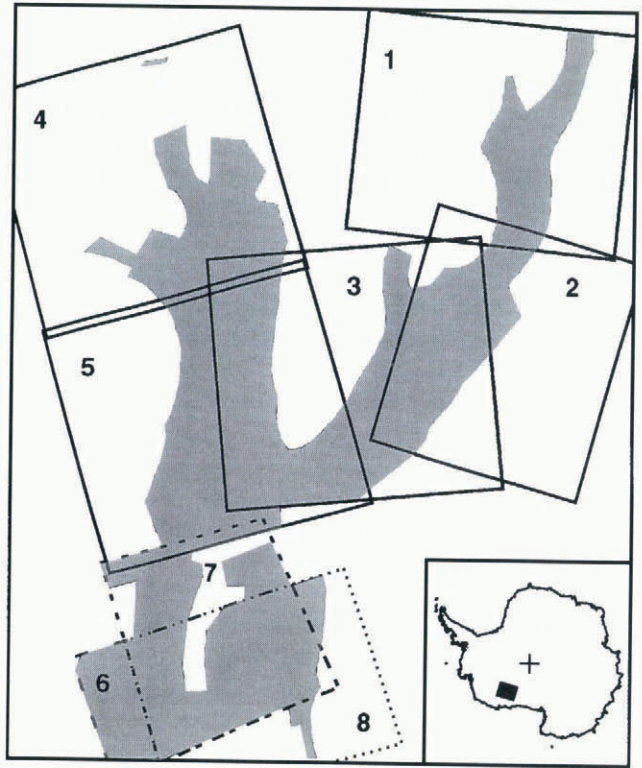


Fig. 2. Location of TM image pairs used in velocity determination. Image ID numbers, acquisition dates and time interval between each image pair are listed in Table 1.

Table 1 provides information on each image (ID number, path/row index numbers and date), as well as the time separation for each image pair. Most of each ice

Table 1. Landsat TM image pairs used for velocity determinations

Area	Scene ID	Path/Row	Acquisition date	Time interval years	No. of vectors	Coreg. error pixels	Coreg. error m a <sup>-1</sup>	Random error pixels	Random error m a <sup>-1</sup>
1	5105014074	233/119	15 Jan 1987	4.906	3537	2.23	12.95	0.49	2.85
	5284214123	233/119	12 Dec 1991						
2	5032913355	226/121	24 Jan 1985	6.880	1522	3.97	16.45	0.52	2.15
	5284214125	233/120	12 Dec 1991						
3	5105114510	007/119	16 Jan 1987	1.906	23 482	1.04	15.55	0.46	6.88
	4234115030	007/119	12 Dec 1988						
4	5105215333	014/117	17 Jan 1987	5.038	8267	3.68	20.82	0.54	3.05
	5289215380	014/117	31 Jan 1992						
5	5105215335	014/118	17 Jan 1987	5.038	20 916	2.85	16.12	0.47	2.66
	5289215383	014/118	31 Jan 1992						
6	5105015464	016/119	15 Jan 1987	3.058	9554	~2.0	18.64	0.34	3.17
	4276116172	019/118	5 Feb 1990						
7	4240615472	014/119	15 Feb 1989	0.972	2273	~2.0	58.64	0.47	13.78
	4276116172	019/118	5 Feb 1990						
8	5105015464	016/119	15 Jan 1987	2.086	5831	~2.0	27.33	0.28	3.83
	4240615472	014/119	15 Feb 1989						

stream is covered by image pairs sharing the same path/row (areas 1, 3, 4 and 5 in Figure 2). One small area on Ice Stream D (area 2) and most of the Ross Ice Shelf region (areas 6, 7 and 8) required a rotation of one image's axes to align its local coordinate system with an overlapping image. Cubic convolution resampling was applied to rotated images. Velocity comparisons in overlap regions, where one image pair included rotation and one did not, indicated that velocity accuracy was not degraded by image rotation.

Computer-memory limitations forced sub-sampling of full-resolution, low-pass filtered images prior to co-registration. This led to larger co-registration errors than would have been achieved with more computer memory. Typical co-registration errors were a few pixels (see Table 1). Because this error is constant for any image pair, it is treated as a systematic error within that image pair. Each cross-correlation match has an additional random error, typically about  $\pm 0.5$  pixel (roughly 14 m) (see Table 1). Velocity errors scale as the inverse of the time separation. Time separation varied for different image pairs from slightly less than 1 year to more than 6 years. Table 1 includes both the systematic and random errors of each image pair.

Velocity points were sought on a regular grid with a spacing of 20 pixels (about 570 m), with more detail attempted in a few smaller areas. Automatic selection criteria were included in the feature-matching process to remove erroneous matches. Each match was also reviewed visually on a computer monitor. Matches that were not consistent with the local flow field were removed. Figure 3 shows the spatial distribution of the final data set consisting of over 75 000 velocity matches.

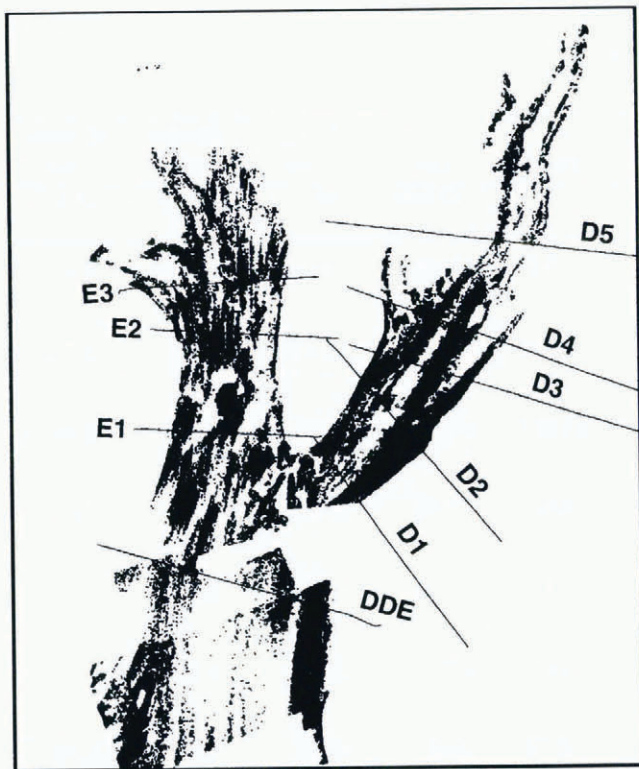


Fig. 3. Positions of 75 382 velocity data points determined by cross-correlation technique and positions and names of airborne transects.

Slowly moving areas had either no features to track (the center of Ice Stream D and parts of the Ross Ice Shelf are examples) or produced velocities with magnitudes comparable to the uncertainties (the ridges between the ice streams are examples). Features in the margins of Ice Stream E experienced so much shear during the 5 year interval between images (areas 4 and 5) that distorted features could not be correlated between images. Unreliable data were deleted during a manual quality check of the data set. Remaining data were gridded to a regular grid with a spacing of 500 m using minimal smoothing. A mask was then applied to eliminate gridding artifacts in the non-ice-stream areas and the non-mapped margins of Ice Stream E. Figure 4 shows the resulting field of surface-velocity magnitude (speed).

Errors in displacement returned by the feature-tracking program were compared with a residual method by which the deviation of each velocity value from its local neighborhood is used as a more traditional measure of velocity error using a root-sum-squared algorithm (Whillans and Tseng, 1995). Comparisons made between the respective errors in the speed component showed no spatial coherence to the differences, but the residual measure of error was uniformly higher than the errors in Table 1 by about 12%. This is acceptable agreement to justify using the errors in Table 1 as standard deviations of velocity for the subsequent calculations of this paper.

### Ice thickness

Ice thickness was measured primarily by airborne ice-penetrating radar. A surface-based profile, completed near the grounding line, provided important additional information to help assess the airborne data. The 60 MHz airborne radar stacked 2048 returns every 0.33 s (Blankenship and others, 1994). After processing, ice-thickness values were spaced every 30 m along ten transects of the ice streams (see Figure 3 for transect locations). The positions of the transects were chosen prior to the velocity determinations based on our assessment of where velocity data would probably be obtainable.

Precision of the radar ice-thickness measurement is estimated at one wavelength or  $\pm 5$  m. Relative elevation precision relied on flying a constant-pressure surface and is estimated at  $\pm 10$  m. Using GPS CA-code differential pseudo-range data, absolute positions of the aircraft are accurate to  $\pm 100$  m. For thickness gradients of  $10^{-2}$ , somewhat higher than average for these ice streams, this positional uncertainty corresponds to an uncertainty of  $\pm 1$  m in ice thickness. Thus, the total random uncertainty in ice thickness is probably less than  $\pm 5.1$  m.

Two checks on the radar-data accuracy are possible. The first is based on the two parallel transects flown across the mouths of Ice Streams D and E. The line separation was maintained at roughly 0.5 km and the mean difference in ice thicknesses was  $0.6 \pm 1.9$  m. The thickness gradient in this area is approximately  $10^{-3}$  averaged over many kilometers. Thus, the precision appears to be well within the estimates stated above. The second check compares the same airborne profiles with a 75 km long profile of ice thickness made using a

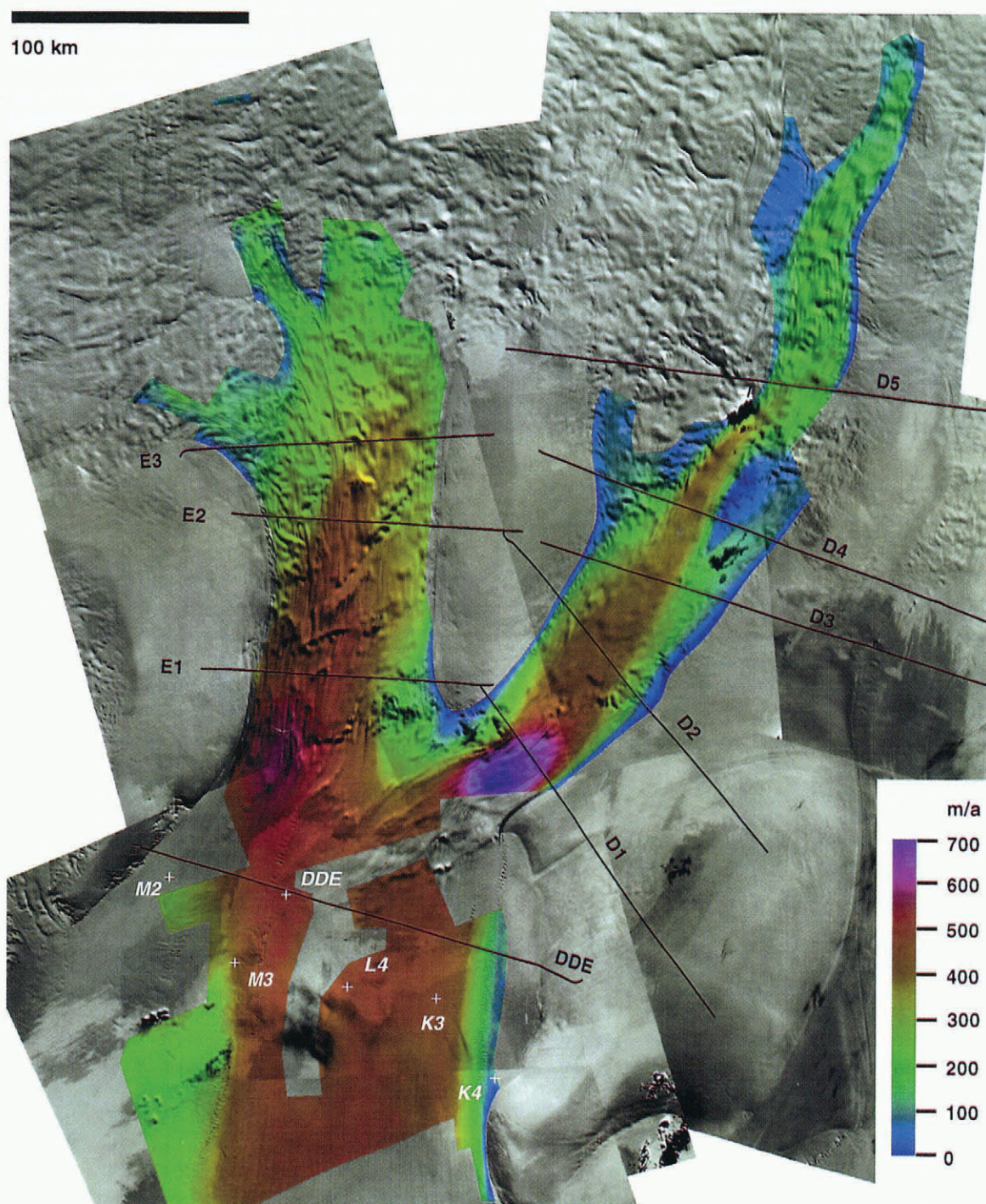


Fig. 4. Color-coded velocity magnitude (speed) superimposed on image mosaic. Transects are shown in black. White crosses show positions of stations discussed in text.

surface-based impulse radio-echo-sounding system (Jacobel and Bindschadler, 1993). Comparing the travel times of the ground-based system with the average of the two airborne systems, the rms. difference was  $4.2 \pm 3.3$  m ice thickness. This is within the uncertainty stated above for a region of low ice-thickness gradient.

The largest contributor to the systematic component of ice-thickness uncertainty is the radar wave speed in ice. Two-way velocity values ranging from 170 to  $178.5 \text{ m } \mu\text{s}^{-1}$  have been reported, based on measurements made throughout the Ross Ice Shelf (Robertson and Bentley, 1984). Jacobel performed a constant midpoint profile experiment at the mouth of Ice Stream D and obtained a

two-way wave speed of  $175 \pm 1 \text{ m } \mu\text{s}^{-1}$  (Jacobel and Bindschadler, 1993). We use this value but assign a systematic error of  $\pm 10$  m for ice thickness.

### Accumulation

In recent years, 29 shallow firn cores have been collected within the catchment areas of Ice Streams D and E, including on the ice streams themselves. Most of these cores have yet to be analyzed for  $\beta$ -particle activity so accumulation-rate data remain sparse for the present. Additional values of accumulation rate were measured from cores of the Ross Ice Shelf, as well as data collected

in snow pits by traversing fields parties during the International Geophysical Year, 1957–58 (Thomas and others, 1984). The data exhibit a large spatial variation with a mean of  $0.11 \text{ kg m}^{-2} \text{ a}^{-1}$ . This mean value is used uniformly in the following analysis with a large uncertainty of  $\pm 0.05 \text{ kg m}^{-2} \text{ a}^{-1}$  to account for expected spatial variations.

It is shown later that the errors in mass balance for sections of Ice Streams D and E are not strongly influenced by even this liberal uncertainty in the accumulation rate. This contrasts with mass-balance calculations over large regions, such as entire ice-stream drainage basins, where accumulation-rate uncertainty can dominate the overall error budget (Whillans and Bindschadler, 1988). Equation (2), presented later, shows that the error contribution of accumulation rate scales with the surface area of the region considered, while the errors in the discharge fluxes do not.

### VELOCITY FIELD

The velocities mapped by image-based feature tracking shown in Figure 4 do not extend far enough upstream to include the area of initial ice-stream formation. The most inland part of Ice Stream D that contains trackable moving features is already moving at a speed of approximately  $130 \text{ m a}^{-1}$ . Byrd Station, moving at only  $13 \text{ m a}^{-1}$ , lies approximately 160 km farther upstream (Whillans and Johnson, 1983). Despite this gap in the incipient ice-stream velocity field, trackable surface features define an initial, well-defined, single tributary of Ice Stream D. Initially 10 km across, this tributary widens slightly after being joined by ice from the north (50 km upstream of gate D5). This single tributary extends 150 km before squeezing through a narrow 10 km wide stricture (between gates D4 and D5), where it accelerates to over  $400 \text{ m a}^{-1}$ . Ice to either side of this main “jet” accelerates (upstream of gate D4), forming a 70 km wide ice stream by gate D3. The faster central flow develops a relatively featureless surface, while slower, adjacent ice exhibits a rough, undulated surface. As gate D2 is passed, transverse velocity gradients near the margins intensify, indicating increasing lateral shear. As gate D1 is approached, a radical lateral flow asymmetry develops: ice decelerates on one side (the north), while ice on the other side (the south) accelerates. This asymmetry is accompanied by a gradual turning of the ice away from the usual center-line parallel direction toward the region of faster ice, where the speed reaches a maximum of nearly  $700 \text{ m a}^{-1}$ . Although flow direction is not shown in Figure 4, it can be discerned from the elongated image features. Again, the fast ice exhibits little surface relief while the slow side of the ice stream has a rough surface. (The basal conditions of this area will be discussed later.) The high speeds in this region are not maintained much beyond gate D1. After Ice Streams D and E join, the stream spreads laterally, with strongly elongated features, until the grounding line is reached (upstream of gate DDE), a distance of less than 100 km. The grounding line can be detected by noting the downstream limit of surface undulations as confirmed by Jacobel and others (1994).

Ice Stream E is fed by a series of adjacent tributaries (upstream of gate E3) spread over a wider region than Ice Stream D. These tributaries coalesce over a shorter longitudinal distance than on Ice Stream D and form a wider trunk flow (75 km at gate E2), compared to the narrow, 10 km wide “jet” upstream of gate D4. Flow speeds above  $400 \text{ m a}^{-1}$  begin downstream of gate E3. Similar to Ice Stream D, ice moving faster than  $400 \text{ m a}^{-1}$  tends to be associated with smoother surface topography than areas of slower ice. Just downstream of gate E1, near the mouth of Ice Stream E, a transverse-flow asymmetry is seen that is similar, but less intense, to that across gate D1. Maximum speeds do not exceed  $550 \text{ m a}^{-1}$ , but the rougher surface is clearly associated with the slower ice. The two slow regions at the Ice Streams D/E confluence may bear some connection to the presence, or even formation, of the nearly stagnant ridge between the ice streams. Downstream from these two slow-flowing, rough-surface regions at the Ice Streams D/E confluence, a broad, very smooth area is evident. This region probably contains thinner ice than upstream, making it likely that it is a confined ice shelf or, as Bamber and Bentley (1994) have suggested, an ice plain, i.e. a region of lightly grounded ice.

On the ice shelf, enough features can be tracked that the general pattern of velocity is discerned. The faster-moving parts of both ice streams join to maintain speeds of over  $400 \text{ m a}^{-1}$  on the ice shelf. Downstream of station M3, numerous ice rises and ice rumples retard the flow there, forcing the major discharge to pass between these features and Siple Dome. The imagery of the slower-moving region, including station M2, north of these ice rises and rumples suggests that it also may be an ice plain. The shearing south margin of the ice shelf, close to Siple Dome, contains parallel sets of crevasses. These crevasse bands are well offset from the grounding line of Siple Dome, forming a large, nearly stagnant embayment, including station K4.

The only independent measurements of ice velocity for comparison with the velocities of Figure 4 occur on the ice shelf. Table 2 presents a time series of the available velocity measurements. Field work at sites K3 and M3 during the Ross Ice Shelf Glaciological and Geophysical Survey (RIGGS) in the mid-1970s measured ice motion using the TRANSIT satellite-navigation system (Thomas and others, 1984). Site DDE was measured in 1991 and 1993 using a combination of the TRANSIT system and the Global Positioning System (GPS), providing a validating measurement nearly contemporaneous with the TM imagery. The availability of an early Landsat Multi-Spectral Scanner (MSS) image greatly extends the time span of the imagery for velocity mapping. The MSS image, acquired in 1973, has lower resolution than TM (pixels 79 m on a side versus 28.5 m for TM); however, the longer time span between the image pair used (16.24 years) results in a relatively low velocity uncertainty. The good agreement of the velocity measurements supports the validity of the image-based technique. The time series shows no clear evidence of velocity change in the mouths of Ice Streams D and E, as was discovered in the mouth of Ice Stream B (Stephenson and Bindschadler, 1988); however, due to the size of the uncertainties, modest changes cannot be ruled out.

Table 2. Comparison of surface velocities on Ross Ice Shelf determined by various methods. n.a. = Not available

	Time interval	DDE	M3	K3
RIGGS	1974–76	n.a.	$414 \pm 15 \text{ m a}^{-1}$	$436 \pm 15 \text{ m a}^{-1}$
MSS*-TM	1973–90	$467 \pm 15 \text{ m a}^{-1}$	$435 \pm 15 \text{ m a}^{-1}$	$417 \pm 15 \text{ m a}^{-1}$
TM-TM (area 8)	1987–89	n.a.	n.a.	$417 \pm 35 \text{ m a}^{-1}$
TM-TM (area 6)	1987–90	n.a.	n.a.	$422 \pm 25 \text{ m a}^{-1}$
TM-TM (area 7)	1989–90	$428 \pm 60 \text{ m a}^{-1}$	$401 \pm 60 \text{ m a}^{-1}$	$443 \pm 60 \text{ m a}^{-1}$
TRANSIT-GPS	1991–93	$469 \pm 2 \text{ m a}^{-1}$	n.a.	n.a.
GPS-GPS	1993 (14d)	$471 \pm 15 \text{ m a}^{-1}$	$395 \pm 15 \text{ m a}^{-1}$	$436 \pm 15 \text{ m a}^{-1}$

\* MSS image 147215300, path 11/row 119, acquired 7 November 1973.

## STRAIN RATES

An additional level of analysis of the velocity field is the determination and interpretation of the strain-rate tensor. This involved a number of steps. Within each of the eight areas (see Fig. 2), the image-axis components,  $D_x$  and  $D_y$ , of the displacements determined by the cross-correlation matching algorithm at each grid point were converted to longitudinal, transverse and shear-strain rates (relative to the local flow direction), as described in the Appendix. These data sets were then spatially smoothed and gridded to a regular 5 km spacing. To map the data sets from each of the eight areas in a single mosaic, each was rotated to a common coordinate system followed by a second spatial smoothing and interpolation to a 5 km grid aligned with the common mosaic coordinate system. To produce a visual display of the surface-horizontal strain rates, each component was bilinearly interpolated to a spacing of 171 m (six TM pixels). These strain-rate images are shown in Figures 5, 6 and 7 with identical color scales.

The choice of 5 km for the grid scale was a compromise between enhancing the signal-to-noise ratio and preserving the significant spatial features of each strain-rate component. Because the strain-rate calculations utilized a centered difference formulation, and the ice streams are almost 1 km thick, this grid spacing averages strain rates over approximately ten ice thicknesses, a large enough distance to remove most of the smaller-scale dynamic effects.

Each velocity data point has uncertainties of the displacements determined by the cross-correlation method. Calculation of the error of each strain-rate component at each data point was accomplished by a straightforward error propagation through each strain-rate equation. These errors were treated in a manner similar to the strain rates themselves, including production of an image of each to evaluate both their magnitude and their spatial pattern. Figure 8 shows the error in longitudinal strain rate. It is lowest on Ice Stream E, highest on the ice shelf and intermediate on Ice Stream D. This spatial signature is primarily due to the respective errors in velocity which are, in turn, a result of the time separation of the image pairs (see Table 1). The patterns for the other strain-rate errors (not shown) are similar, with the magnitudes of longitudinal and transverse strain-rate errors slightly higher than shear strain-rate error. The mean errors for longitudinal, transverse and shear strain rates are  $2.1 \times 10^{-3}$ ,

$2.1 \times 10^{-3}$  and  $1.5 \times 10^{-3} \text{ a}^{-1}$ , respectively.

The mean value of longitudinal strain rate (see Fig. 5) is  $1 \times 10^{-3} \text{ a}^{-1}$ , consistent with the overall acceleration of about  $400 \text{ m a}^{-1}$  over a 400 km distance along the ice streams. The distribution of values has a standard deviation of  $3 \times 10^{-3} \text{ a}^{-1}$  and Figure 5 shows a large degree of spatial coherence that is easily interpretable in terms of the kinematics of the ice streams. Zones of extreme tension are located in acceleration zones where ice is drawn into the ice stream either from the side (see the south margin of Ice Stream D) or from slow-moving areas between tributaries (see the upstream areas of Ice Stream E). The slow-moving region to the north of the confluence point of Ice Streams D and E is marked by a matched pair of upstream compression and downstream tension. On Ice Stream D, the predominant signature in

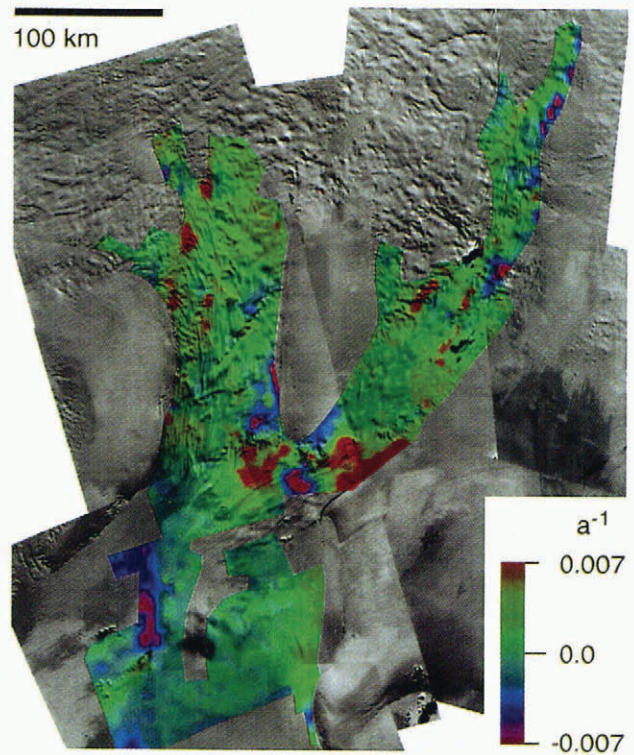


Fig. 5. Longitudinal strain rate (color) calculated from velocity data as described in text. Spatial distribution of errors is shown in Figure 8.

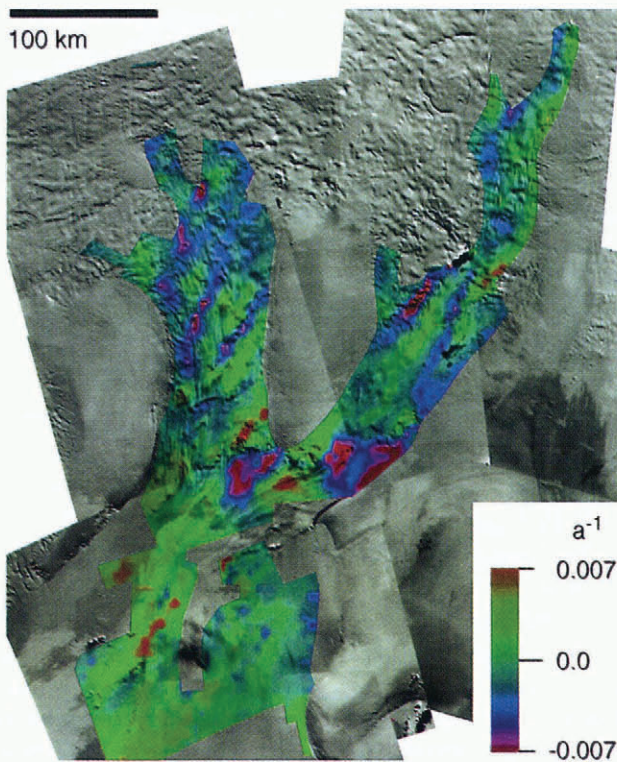


Fig. 6. Transverse strain rate (color) calculated from velocity data as described in text. Spatial distribution of errors is very similar to that shown in Figure 8.

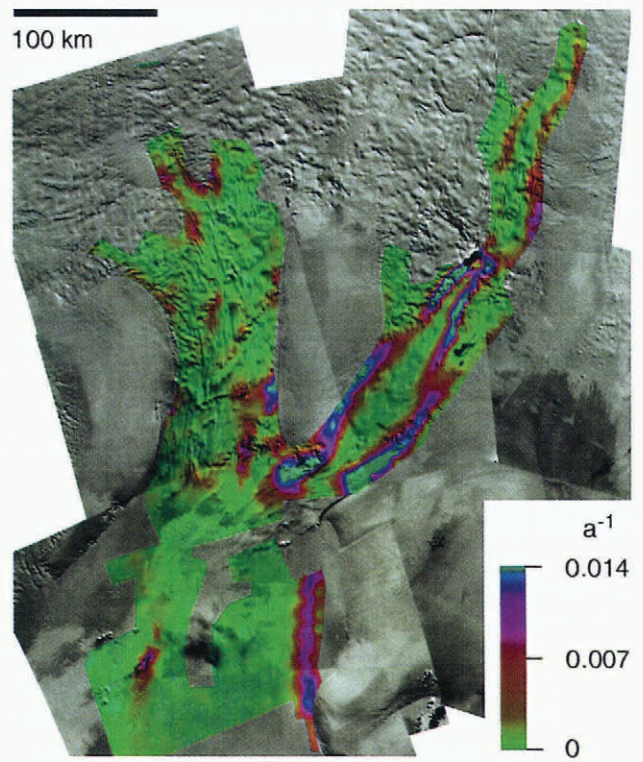


Fig. 7. Shear strain-rate magnitude (color) calculated from velocity data as described in text. Spatial distribution of errors is very similar to that shown in Figure 8.

this confluence region is an upstream acceleration/downstream compression doublet tied to the rapid velocity changes that occur in the southern half of the ice stream. On the ice shelf, the compression upstream of the ice-rise/ice-rumple area is the only significant feature which stands out above the higher errors in this area (see Fig. 8). A final feature worth noting is the longitudinal compression seen on both edges of the 10 km wide stricture through which the narrow Ice Stream D tributary flows before being joined by other tributaries.

Transverse strain rates, shown in Figure 6, have a mean of only  $-0.3 \times 10^{-3} \text{ a}^{-1}$  but a standard deviation of  $3 \times 10^{-3} \text{ a}^{-1}$  (identical to longitudinal strain rate). Lateral compression occurs in most confluence areas (see the upper parts of Ice Stream E and the region on Ice Stream D where adjacent ice joins the single jet). In the region near the confluence of Ice Streams D and E, Ice Stream D experiences compression upstream of the region of maximum speed, where ice converges into this faster area. On Ice Stream E, in the slow area adjacent to the confluence, extension is evident upstream, followed by compression downstream. On the ice shelf, the longitudinal compression associated with the ice rises is also the site of transverse extension as ice diverges around these slower-moving areas. In general, transverse strain rate tends to be the inverse of longitudinal strain rate. Two very interesting exceptions to this relationship are the two obliquely striking regions of transverse compression found near the mid-section of Ice Stream E. These are discussed more fully below in terms of the vertical strain rate.

Shear-strain-rate magnitude, shown in Figure 7,

clearly illustrates the shear margins of Ice Stream D and the south margin of the Ross Ice Shelf. Velocities in the margins of Ice Stream E could not be tracked, as discussed

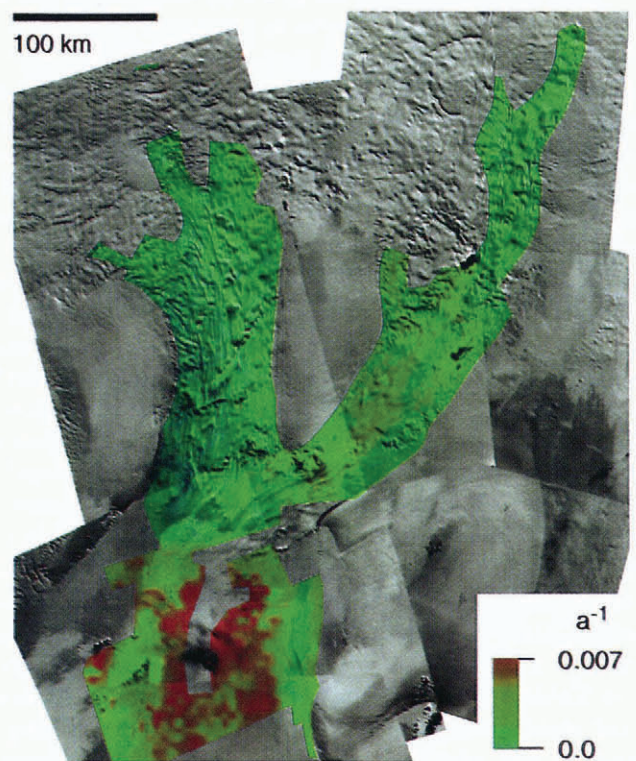


Fig. 8. Error (one- $\sigma$ ) in longitudinal strain rate (color).

earlier, and fall outside the region presented in these figures, but high shear at the sides of some of the tributaries is still apparent. There is also prominent shear associated with the two areas of slow-moving ice at the Ice Streams D/E confluence. Even without the inclusion of Ice Stream E's margins, the mean value is  $3.1 \times 10^{-3} \text{ a}^{-1}$  and the distribution has a standard deviation of  $3.7 \times 10^{-3} \text{ a}^{-1}$ .

The components of principal strain rates and the rotation rate have also been calculated but are not shown. We have confirmed that source regions of crevasses identifiable on the imagery occur where the tensile stress is largest and that the orientations of these new crevasses agree reasonably well with orientations of the most tensile

principal strain rate.

Surface strain rates can also be used to calculate vertical strain rate by applying the continuity condition:

$$\dot{\epsilon}_z = -\dot{\epsilon}_l - \dot{\epsilon}_t. \quad (1)$$

While this is strictly the vertical strain rate at the surface, it is reasonable to assume that this is a good approximation to the depth-averaged vertical strain rate due to the low vertical variation of velocity in ice streams (unpublished borehole results of B. Kamb and H. Engelhardt). Figure 9 shows this strain-rate component. It is printed at a larger scale to assist in identifying correlations between

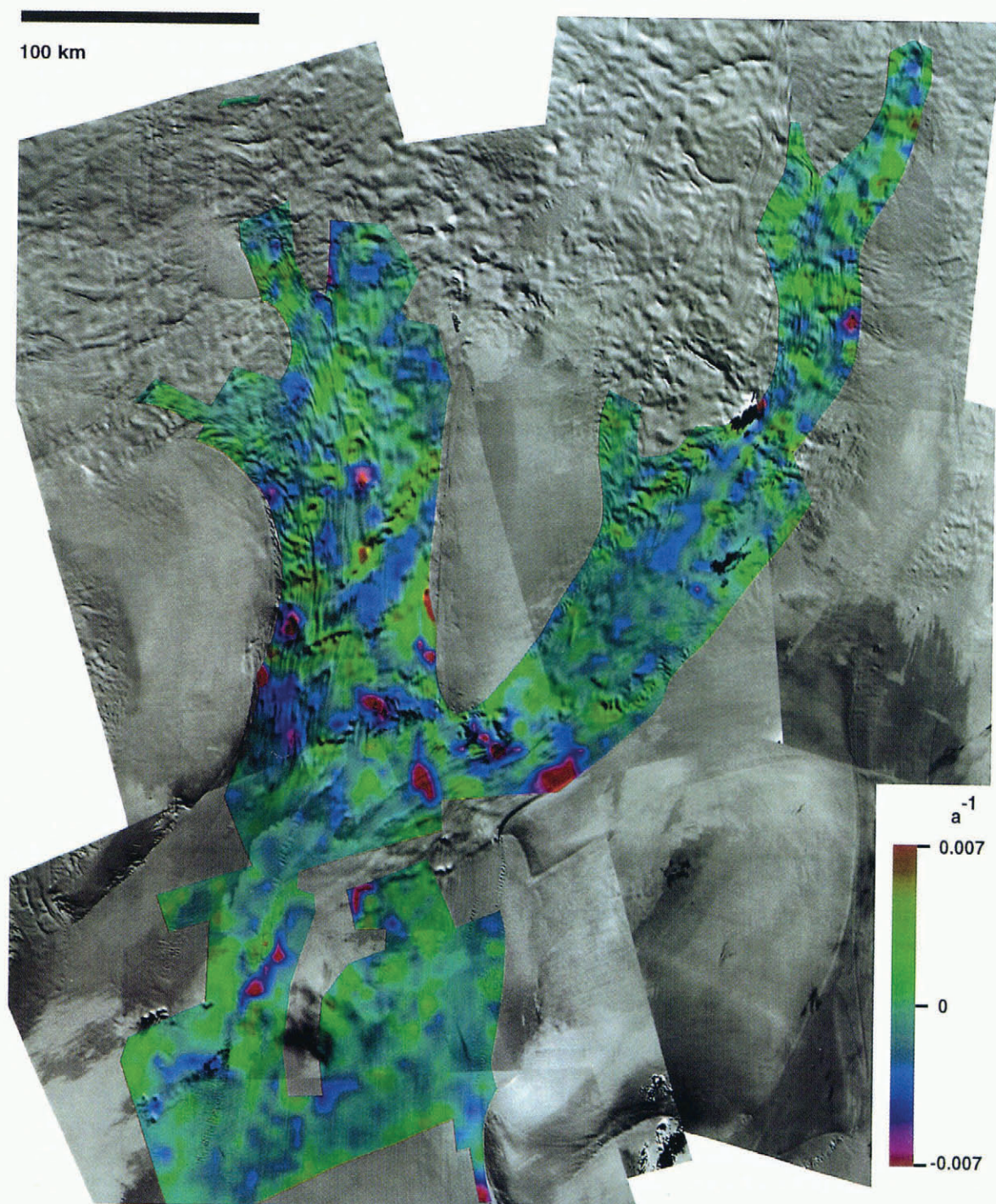


*Fig. 9. Color-coded vertical strain rate superimposed on image mosaic. Spatial distribution of errors is very similar to that shown in Figure 8.*

the vertical strain rate and surface topography. The mean value is  $-0.8 \times 10^{-3} \text{ a}^{-1}$ , representing the overall thinning of the ice as it flows seaward.

Areas of positive vertical strain rate are thickening and correlate extremely well with those areas where rougher surface topography is apparent in the image. MacAyeal and others (1995) found that on Ice Stream E the regions of greater surface relief also corresponded to regions of large basal stress. From Figure 9, a typical rate of vertical extension in these areas is  $4 \times 10^{-3} \text{ a}^{-1}$ . At speeds of  $500 \text{ m a}^{-1}$  and an ice thickness of 1000 m, this corresponds to a thickness gradient of only  $8 \times 10^{-3}$ . Over a 5 km distance, the total thickening amounts to 40 m. This is approximately the same relief scale of the undulations in the rough areas estimated from brightness variations of the imagery (Bindschadler and Vornberger, 1994). Thus, basal relief is not required to explain the surface relief.

If bed relief is present in these areas, there are various models of how it would be related to surface relief. The rigid-column model, where the surface topography exactly matches the bed topography, clearly does not apply, because vertical strain rates are identically zero in this model and the data indicate non-zero vertical strain rates. Plane-strain models (zero transverse strain) require that undulations in surface topography occur one-quarter wavelength upstream from the corresponding bed undulations (Budd, 1970). In this class of models, positive vertical strain occurs primarily in the trough of the surface undulations, with the location of the maximum positive vertical strain rate dependent upon the relative magnitudes of the surface and bed undulations. This signature does not fit the data either. In general, in the regions of positive vertical strain rate, the transverse strain rate exceeds the longitudinal strain rate, further suggesting that plane-strain simplifications are not appropriate.

We suggest the cause of the rougher surface regions is a local increase of the basal friction, that the bed relief is not an exaggerated expression of what is seen on the surface, and that the vertical strain rates are accommodated by the surface topography alone. If the vertical relief is insufficient to account for the entire vertical strain rate, excess positive vertical strain would require that the bed dip more steeply in the downstream direction. This would decrease local water pressure at the subglacial bed (the gravitational potential supplying a greater fraction of the pressure gradient required to transport basal water) and reduce basal lubrication. The result still would be increased basal friction.

While the thickening/rough-surface correlation discussed above is by far the more common situation observed on Ice Streams D and E, there are instances where a rough surface corresponds to a high thinning rate (red in Fig. 9). One of the more prominent occurrences of this is within the upstream region of Ice Stream E, where there is a single, large surface bump coincident with a local thinning maximum. Another area of large thinning is near the Ice Streams D/E confluence, where thinning takes place over both slow-moving, rough areas and farther downstream. The latter case may be similar to the local thinning over a bedrock step reported for Rutford Ice Stream by Frölich and others (1987).

## DISCHARGE FLUXES

The purpose of the airborne ice-thickness data was to facilitate calculation of discharge flux at a series of transverse transects (or "gates") along each ice stream to investigate the longitudinal variation of net mass balance. This technique proved effective in illustrating the dynamic behavior of Ice Stream B (Shabtaie and others, 1988). Co-registration of the airborne data and the imagery was performed, based on geographic coordinates. As mentioned earlier, airborne-data location is from GPS CA-code differential pseudo-range data collected on the aircraft. These data have a standard deviation better than  $\pm 100 \text{ m}$ . Image coordinates were provided by the U.S. Geological Survey, based on a multi-image adjustment using ground-control points distributed primarily in northern Marie Byrd Land with the addition of a few points on or near ice streams, and are accurate to  $\pm 600 \text{ m}$  (Ferrigno and others, 1994). Thus, the accuracy of the co-registration is better than  $\pm 608 \text{ m}$ .

Figure 10 shows the surface and bed elevations along each transect, together with velocity data within 1 km of the transect. Comparison of surface-elevation profiles with surface features seen in the imagery support a co-registration accuracy at least as good as that stated above. Gates are numbered starting at the downstream end of each ice stream (five on Ice Stream D and three on Ice Stream E; see Fig. 1). Gate DDE refers to one of the two transects across the grounding-line area of both ice streams. Velocity data in Figure 10 refer to the velocity component perpendicular to the transect.

Beginning on Ice Stream D, the most upstream gate (D5) is narrow due to the limited amount of velocity data in the most active tributary. The bed topography of gate D5 is generally rougher than for other gates but, over the active tributary, the bed is smoother than the surrounding terrain. Average ice thickness is over 1400 m in the tributary. The boundaries of the channel are not obvious from the basal topography—a characteristic of Ice Streams B and C noted by Shabtaie and Bentley (1987). The main jet is clear in the gate D4 data with a slightly elevated surface but, again, with no basal topographic control to its boundaries. By gate D3, the ice stream has widened and the bed is smoother—not just beneath the ice stream but also under the ridge to the south (toward Ice Stream C). Near the south margin of the ice stream along gate D2, there is a broad, flat-topped basal feature underlying a rough-ice surface. Profiles at D2 and DDE show ice thickness rather than surface and bed topography; however, the surface is much smoother than the bed, so gross features in ice thickness correspond to bed features. The rough surface near the southern margin can be seen in the imagery. Gate D1 captures the transverse asymmetry of the velocity field. The bed is about 10% higher over the faster part of this gate, but this is not nearly enough to compensate for the factor-of-4 difference in speed between the northern and southern parts of the ice stream. Thus, the ice flux is much greater through the faster region despite the reduced ice thickness there.

The transects of Ice Stream E begin upstream with a rough bed and large surface relief at gate E3. The velocity profile indicates an incipient tributary to the north as well

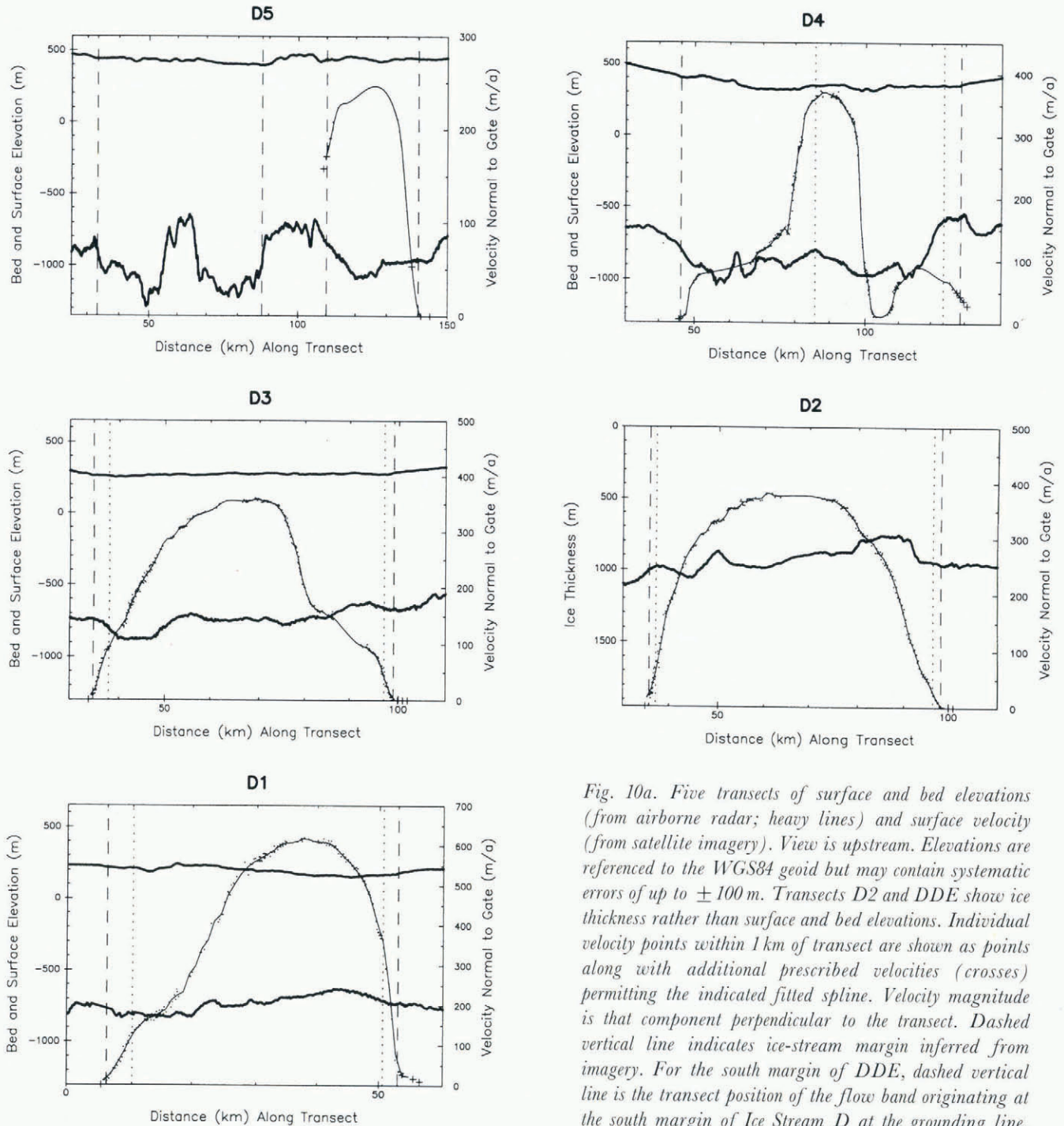


Fig. 10a. Five transects of surface and bed elevations (from airborne radar; heavy lines) and surface velocity (from satellite imagery). View is upstream. Elevations are referenced to the WGS84 geoid but may contain systematic errors of up to  $\pm 100$  m. Transects D2 and DDE show ice thickness rather than surface and bed elevations. Individual velocity points within 1 km of transect are shown as points along with additional prescribed velocities (crosses) permitting the indicated fitted spline. Velocity magnitude is that component perpendicular to the transect. Dashed vertical line indicates ice-stream margin inferred from imagery. For the south margin of DDE, dashed vertical line is the transect position of the flow band originating at the south margin of Ice Stream D at the grounding line. Dotted vertical line indicates the position of the “gate-limited” width as defined in the text.

as two other broad tributaries that fully coalesce downstream of this profile. Gate E2 shows three distinct flows, signaling disruptions upstream of what had been a more uniform flow. These disruptions do not match basal topography at gate E2 and are probably caused by variations in basal friction (discussed earlier). The overall channel roughly matches the full width of the ice stream. Gate E1 illustrates a more uniform flow, albeit with a slower part to the south. At the southern boundary, the bed is remarkably smooth, yet this area is the slowest part of this profile. Finally, at gate DDE (only one of the two profiles is shown), the ice has begun floating, so that the bed shown is no longer the basal topography but the bottom of the ice shelf. This is not true outside the ice stream, where the surface topography rises rapidly and

the bed is much rougher.

Airborne data along each transect were sub-sampled at a constant spacing. Figure 10 illustrates that velocity data are not as uniformly spaced. To facilitate the ice-flux computation, each velocity profile was approximated by a cubic spline. In regions with large gaps in velocity data and near ice-stream margins, velocity estimates were sometimes included to guide the spline and avoid unconstrained velocity variations. These artificial points were kept consistent with other velocity data and with our interpretation of the margin position in the imagery.

If basal stress is absent, the shape of a transverse velocity profile should fit a fourth-order polynomial. There are a few locations where the velocity data of Figure 10 meet this criterion; e.g. the south side of the jet

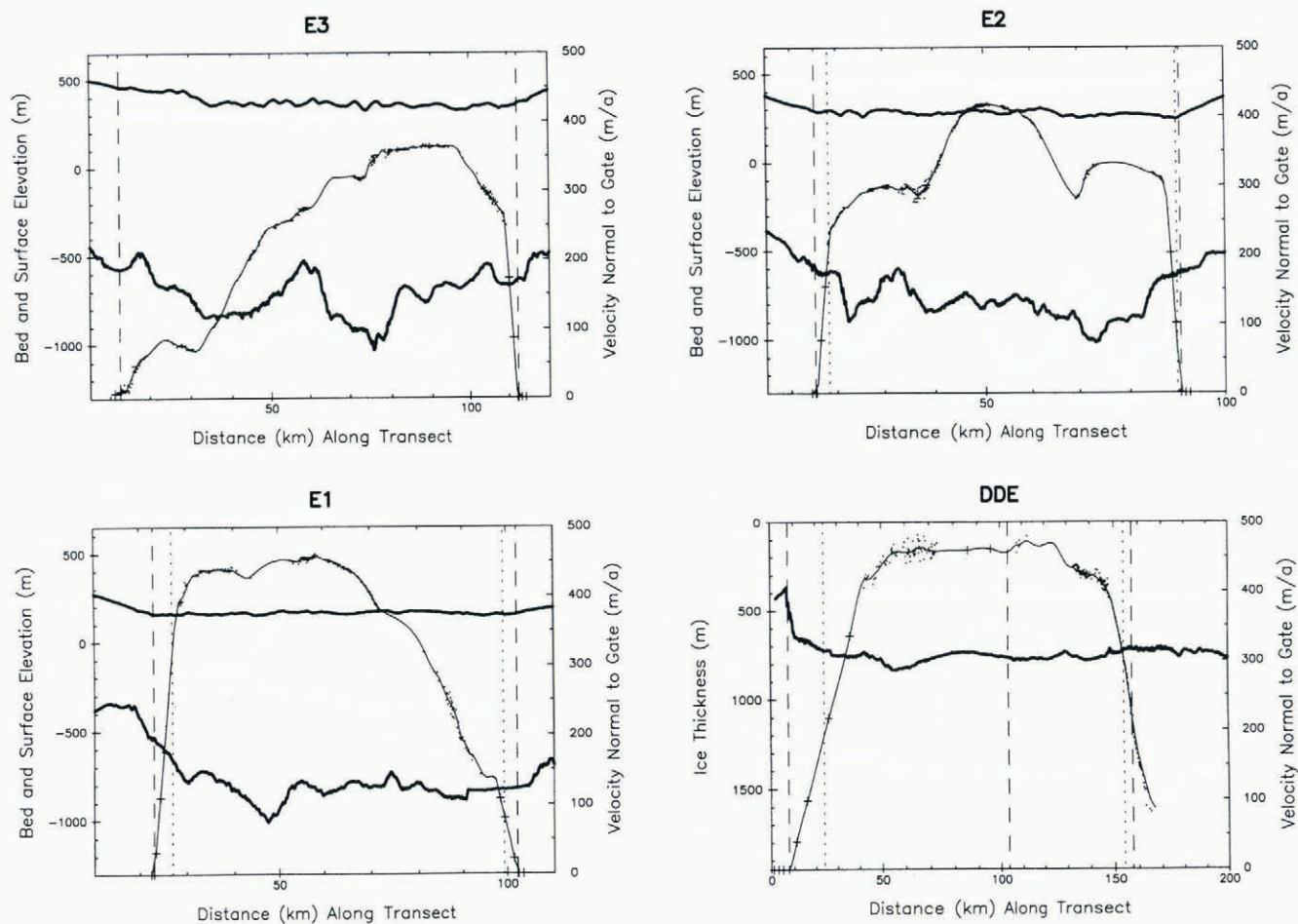


Fig. 10b. Four transects of surface and bed elevations (from airborne radar; heavy lines) and surface velocity (from satellite imagery). See Fig. 10a for description.

at gate D4, north side of gate D2, south side of gate D1, and north side of gate E2. In general, there are significant departures from the fourth-order polynomial shape, indicating large variations in the forces resisting ice-stream flow.

With continuous profiles of velocity and ice thickness across each transect, the ice-equivalent volume flux,  $F$ , for each transect was calculated in 1 km increments across the full width using the formula:

$$F = \sum_W V_t(H - C)\Delta w \quad (2)$$

where  $W$  is the width,  $V_t$  is the velocity component perpendicular to the transect,  $H$  is the ice thickness,  $C$  is the equivalent thickness of air in the ice column and  $\Delta w$  is the increment of width. Two key assumptions are made in this calculation. The first is that there is no velocity variation with depth. This is valid on these ice streams, where driving stress is low yet velocity is high. Sliding or till deformation must dominate with negligible internal deformation. The second assumption is that  $C$  is constant and equal to 12 m of ice equivalent (Alley and Bentley, 1988). The calculated fluxes, together with the average values of gate-perpendicular velocity ( $\bar{V}_t$ ) and ice thickness ( $\bar{H}$ ), appear in Table 3. (Note that the product  $\bar{V}_t(\bar{H} - C)W$  will not, in general, equal the gate fluxes in

Table 3.)

A considerable volume of ice flows into the ice streams from the sides, yet accurate values of either ice thickness or ice velocity along the margins are not available. To account for this lateral influx of ice, the lateral limits of the flow from each gate were traced downstream to the next gate by following flow bands in the images. We refer here to this narrower width as the “gate-limited” width. If flow is steady, no ice should flow across these longitudinal features. In support of this approach, no cases were encountered where the flow-band orientation was not parallel to the measured flow direction. “Gate-limited” fluxes ( $F'$ ) were calculated using Equation (2) (where the “gate-limited” width,  $W'$ , is substituted for the full width) for all gates except the most upstream gates, D5 and E3 (see Table 3).

As a check on the contribution of transverse flow across the ice-stream margins, the difference between the “gate-limited” flux and the full flux was converted to a transverse “cross-margin” velocity using appropriate data of ice thickness and distances from Figures 4 and 10. Along all but one margin segment, the “cross-margin” velocity was less than  $8 \text{ m a}^{-1}$ . These are consistent with velocities at the margin of Ice Stream B (Whillans and Van der Veen, 1993). The only exception was  $14 \text{ m a}^{-1}$  across the northern boundary between gates E1 and DDE where flow bands show considerable inflow. Precise

Table 3. Discharge fluxes (ice-equivalent) and average rates of thickness change for Ice Streams D and E. Data for each gate include width, average values of velocity and ice thickness, and ice-equivalent mass flux computed from Equation (2) using profiles of velocity and ice thickness (Fig. 10). Parentheses and asterisks indicate reduced uncertainties achievable when velocity data occur on the same image pair as discussed in the text. Accumulation flux is calculated from assumed constant rate of  $0.11 + 0.05 \text{ kg m}^{-2}$  and the indicated surface area between gate pairs. Rate of thickness change is calculated from Equation (3)

Gate	<i>W</i>	$\bar{V}_t$	$\bar{H}$	Flux	“Gate-limited” flux	Accumulation flux	Surface area	Rate of thickness change
	km	$\text{m a}^{-1}$	m	$\text{km}^3 \text{ a}^{-1}$	$\text{km}^3 \text{ a}^{-1}$	$\text{km}^3 \text{ a}^{-1}$	$\text{km}^2$	$\text{m a}^{-1}$
<i>Ice Stream D</i>								
D5	30.1	194.1	1432.7	$8.66 \pm 0.66$		$0.21 \pm 0.11$	2102.7	<b><math>0.86 \pm 0.53</math></b>
D4	82.5	138.1	1220.2	$13.89 \pm 1.83$ ( $\pm 0.25$ )	$7.07 \pm 0.88$	$0.23 \pm 0.12$	2296.7	<b><math>-0.21 \pm 0.15^*</math></b>
D3	64.2	222.3	1017.7	$14.81 \pm 1.26$ ( $\pm 0.23$ )	$14.60 \pm 1.17$ ( $\pm 0.22$ )	$0.22 \pm 0.11$	2236.7	<b><math>-0.31 \pm 0.16^*</math></b>
D2	62.5	275.0	912.0	$15.81 \pm 1.16$ ( $\pm 0.26$ )	$15.72 \pm 1.11$ ( $\pm 0.26$ )	$0.26 \pm 0.13$	2578.1	<b><math>-0.02 \pm 0.16^*</math></b>
D1	46.8	399.8	927.2	$16.80 \pm 0.99$	$16.11 \pm 0.89$ ( $\pm 0.30$ )	$0.46 \pm 0.23$	4632.3	<b><math>0.13 \pm 0.43</math></b>
DDE/D	53.8	426.5	760.8	$17.53 \pm 1.84$	$16.65 \pm 1.73$			
				$22.5 \pm 1.9$ (Shabtaie and Bentley, 1987)				
<i>Ice Stream E</i>								
E3	99.9	234.9	1091.8	$25.64 \pm 2.37$		$0.28 \pm 0.14$	2752.8	<b><math>0.22 \pm 1.03</math></b>
E2	75.35	314.0	1063.0	$25.64 \pm 1.59$ ( $\pm 0.30$ )	$25.32 \pm 1.53$	$0.46 \pm 0.23$	4637.9	<b><math>-0.02 \pm 0.11^*</math></b>
E1	79.28	340.7	975.9	$26.76 \pm 1.61$	$26.12 \pm 1.50$ ( $\pm 0.35$ )	$0.71 \pm 0.36$	7096.4	<b><math>0.44 \pm 0.27</math></b>
DDE/E	96.0	361.7	746.8	$26.51 \pm 1.19$	$24.34 \pm 1.01$			
				$26.2 \pm 2.4$ (Shabtaie and Bentley, 1987)				

magnitudes of these velocities are not significant given the errors in the fluxes.

Flux errors were calculated by propagating the errors of the velocity and ice thickness through Equation (2). In general, systematic errors dominate. Random errors were minimized by the large number of data available from the remote-sensing methods. Surface area and accumulation flux also appear in Table 3, completing the necessary data to compute the rate of thickness change.

**MASS BALANCE**

The mass balance for any region bounded by two gates follows directly from summing the upstream gate flux and the accumulation flux and subtracting the downstream gate flux (using the gate-limited value to avoid account-

ing for lateral fluxes). This can then be converted to a rate of thickness change:

$$\Delta H / \Delta t = (F - F' + A) / S \tag{3}$$

where  $\Delta H / \Delta t$  is the rate of thickness change,  $F$  is the upstream mass flux,  $F'$  is the downstream “gate-limited” flux,  $A$  is the accumulation flux and  $S$  is the ice-stream surface area.

A significant reduction in error occurs when the two gates occur on the same image pair. In this case, the systematic image-co-registration error can be ignored. These cases are indicated in Table 3 by parentheses enclosing the lower flux errors and by an asterisk following the calculated rates of thickness change.

The data reveal that, while Ice Streams D and E appear to be in overall equilibrium in the region studied,

there is evidence of local thinning and thickening. Ice Stream D is thickening at the upper end of the calculated region (gates D5 to D4), thinning slightly between gates D4 and D1, and perhaps thickening downstream of gate D1. The most statistically significant imbalance is between gates D3 and D2 but, even there, the thinning is only two standard deviations from zero. The largest imbalance occurs in the most upstream region, but it also contains the largest error due to the smaller surface area and the fact that gates D4 and D5 are on different image pairs. On Ice Stream E, the only region identified as significantly out of balance is the most downstream (gates E1 to DDE) but, again, the difference is only two standard deviations from zero.

Jacobel and Bindschadler (1993) measured ice thickness at K3 and M3 (see Fig. 4) and found a thickening of  $14 \pm 11$  m in 16 years. The earlier discussion of geociever- and image-derived velocities in this area (see Table 2) left open the possibility of a decrease in speed at these locations over this same time interval. These two sites lie downstream of the most downstream mass-balance region in the mouths of Ice Streams D and E. A thickening might well result in a deceleration, but the rates of both are much lower than what has been documented on Ice Stream B (Stephenson and Bindschadler, 1988; Bindschadler and others, 1993).

#### COMPARISON WITH PREVIOUS DISCHARGE-FLUX ESTIMATES

The discharge fluxes of Ice Streams D and E in Table 3 can be compared with those calculated by Shabtaie and Bentley (1987) at a transverse position approximately 40 km downstream. Our value for Ice Stream D is  $17.53 \pm 1.84$  km<sup>3</sup> a<sup>-1</sup>, lower than their value of  $22.5 \pm 1.9$  km<sup>3</sup> a<sup>-1</sup>, while for Ice Stream E our value of  $26.51 \pm 1.19$  km<sup>3</sup> a<sup>-1</sup> is in excellent agreement with their flux of  $26.2 \pm 2.4$  km<sup>3</sup> a<sup>-1</sup>. Our calculations of Ice Stream D's discharge amount to a 22% reduction in flux and modifies Shabtaie and Bentley's resulting net flux of Ice Stream D (discharge flux minus accumulation flux) downward by 70% to  $2.3 \pm 3.6$  km<sup>3</sup> a<sup>-1</sup>, a figure that is much closer to equilibrium.

A comparison of their velocity data with ours reveals the cause of the discrepancy on Ice Stream D. Their velocity profile across the two ice streams was based on only two directly measured velocities (at K3 and M3; see Table 2) and three velocities (at K4, L4 and M2) interpolated from measured velocity and strain-rate data at nearest-neighbor stations (Thomas and others, 1984). For the stations in the path of Ice Stream D, the interpolated RIGGS velocity of  $465 \pm 30$  m a<sup>-1</sup> at L4 agrees well with our value of  $442 \pm 6$  m a<sup>-1</sup>; however, Figure 4 shows that K4 lies in the stagnant embayment adjacent to Siple Dome. The intense marginal gradient of velocity between K3 and K4 would have not been detected by strain-rate measurements at these stations alone. Clearly, the proper velocity at K4 is much less than the interpolated RIGGS value of  $325 \pm 30$  m a<sup>-1</sup>. To a lesser degree, the RIGGS interpolated velocity of  $165 \pm 30$  m a<sup>-1</sup> at M2 appears to be too low, although this station lies just beyond the area of velocity coverage.

#### CONCLUSION

The utilization of high-resolution satellite imagery for mapping the velocity field of entire ice streams has obvious relevance to studies seeking to understand the dynamic behavior of ice sheets. Accuracies are comparable to satellite-positioning surveys of just a few years ago. More precise positions can now be obtained using GPS, but spatial-coverage limitations are obvious. Ice Streams D and E provide excellent examples of the complexity of ice-stream flow and the addition of velocity information significantly enhances the ability to interpret the surface features revealed by the imagery in terms of ice-stream kinematics.

Most of the areas of Ice Streams D and E moving faster than 100 m a<sup>-1</sup> have been mapped for velocity. Both ice streams exhibit coalescing tributaries, but Ice Stream D comprises longer, narrower sections; the central part nearly devoid of surface features probably experiences little basal friction. Ice Stream E has a shorter, wider trunk and probably a more spatially variable pattern of basal friction. Both ice streams exhibit a marked asymmetry at their confluence, with Ice Stream D's flow diverted the most. Vertical strain rates correlate with surface relief in a manner that suggests rougher surface relief can serve as a proxy indicator for regions of increased basal friction.

The combination of these remote-sensing data sets with airborne remote sensing of ice thickness enables the calculation of the spatial pattern of mass balance. The density of data minimizes the random errors, but systematic errors continue to limit the ability of the technique to resolve extremely local variations in mass balance. These limitations are eased considerably when the region is contained completely on only one time-separated image pair. Our calculations improve an earlier estimate of the net mass balance for Ice Stream D (Shabtaie and Bentley, 1987) and indicate that, while both Ice Streams D and E are in approximate equilibrium, some local variations in mass balance probably exist.

#### ACKNOWLEDGEMENTS

The collection and analysis of these data required the energies of many persons who do not appear as authors. M. Fahnstock provided a wealth of expertise and good advice at many stages of this research. R. Bell oversaw the GPS positioning of the aircraft that was a major factor in limiting the position-related errors. Financial support was provided by U.S. National Science Foundation grants OPP-9018127 and OPP-9317627.

#### REFERENCES

- Alley, R. B. and C. R. Bentley. 1988. Ice-core analysis on the Siple Coast of West Antarctica. *Ann. Glaciol.*, **11**, 1–7.
- Bamber, J. and C. R. Bentley. 1994. A comparison of satellite-altimetry and ice-thickness measurements of the Ross Ice Shelf, Antarctica. *Ann. Glaciol.*, **20**, 357–364.
- Bindschadler, R. A. and T. A. Scambos. 1991. Satellite-image-derived velocity field of an Antarctic ice stream. *Science*, **252**(5003), 242–246.
- Bindschadler, R. A. and P. L. Vornberger. 1994. Detailed elevation map

of Ice Stream C, Antarctica, using satellite imagery and airborne radar. *Ann. Glaciol.*, **20**, 327–335.

Bindschadler, R., P. L. Vornberger and S. Shabtaie. 1993. The detailed net mass balance of the ice plain on Ice Stream B, Antarctica: a geographic information system approach. *J. Glaciol.*, **39**(133), 471–482.

Blankenship, D. D., R. E. Bell and CASERTZ Group. 1994. Corridor aerogeophysics in the interior Ross Embayment of West Antarctica. *Terra Antarctica*, **1**(3), 507–508.

Budd, W. F. 1970. Ice flow over bedrock perturbations. *J. Glaciol.*, **9**(55), 29–48.

Ferrigno, J. G. and 7 others. 1994. Landsat TM image maps of the Shirase and Siple Coast ice streams, West Antarctica. *Ann. Glaciol.*, **20**, 407–412.

Frolich, R. M., D. R. Mantripp, D. G. Vaughan and C. S. M. Doake. 1987. Force balance of Rutford Ice Stream, Antarctica. *International Association of Hydrological Sciences Publication* 170 (Symposium at Vancouver 1987—*The Physical Basis of Ice Sheet Modelling*), 323–331.

Jacobel, R. W. and R. Bindschadler. 1993. Radar studies at the mouths of Ice Streams D and E, Antarctica. *Ann. Glaciol.*, **17**, 262–268.

Jacobel, R. W., A. E. Robinson and R. A. Bindschadler. 1994. Studies of the grounding-line location on Ice Streams D and E, Antarctica. *Ann. Glaciol.*, **20**, 39–42.

MacAyeal, D. R., R. A. Bindschadler and T. A. Scambos. 1995. Basal friction of Ice Stream E, West Antarctica. *J. Glaciol.*, **41**(138), 247–262.

Nye, J. F. 1959. A method of determining the strain-rate tensor at the surface of a glacier. *J. Glaciol.*, **3**(25), 409–419.

Robertson, J. D. and C. R. Bentley. 1984. Seismic studies on the grid-western half of the Ross Ice Shelf RIGGS I and RIGGS II. In Hayes, D. and C. R. Bentley, eds. *The Ross Ice Shelf: glaciology and geophysics*. Washington, DC, American Geophysical Union, 55–86. (Antarctic Research Series 42.)

Scambos, T. A. and R. A. Bindschadler. 1991. Feature maps of Ice Streams C, D and E, West Antarctica. *Antarct. J. U.S.*, **26**(5), 312–314.

Scambos, T. A., M. J. Dutkiewicz, J. C. Wilson and R. A. Bindschadler. 1992. Application of image cross-correlation to the measurement of glacier velocity using satellite image data. *Remote Sensing Environ.*, **42**(3), 177–186.

Shabtaie, S. and C. R. Bentley. 1987. West Antarctic ice streams draining into the Ross Ice Shelf: configuration and mass balance. *J. Geophys. Res.*, **92**(B2), 1311–1336. (Erratum: *J. Geophys. Res.*, 1987, **92**(B9), 9451.)

Shabtaie, S., C. R. Bentley, R. A. Bindschadler and D. R. MacAyeal. 1988. Mass-balance studies of Ice Streams A, B, and C, West Antarctica, and possible surging behavior of Ice Stream B. *Ann. Glaciol.*, **11**, 137–149.

Stephenson, S. N. and R. A. Bindschadler. 1988. Observed velocity fluctuations on a major Antarctic ice stream. *Nature*, **334**(6184), 695–697.

Thomas, R. H., D. R. MacAyeal, D. H. Eilers and D. R. Gaylord. 1984. Glaciological studies on the Ross Ice Shelf, Antarctica, 1973–1978. In Hayes, D. and C. R. Bentley, eds. *The Ross Ice Shelf: glaciology and geophysics*. Washington, DC, American Geophysical Union, 21–53. (Antarctic Research Series 42.)

Whillans, I. M. and R. A. Bindschadler. 1988. Mass balance of Ice Stream B, West Antarctica. *Ann. Glaciol.*, **11**, 187–193.

Whillans, I. M. and S. J. Johnsen. 1983. Longitudinal variations in glacial flow: theory and test using data from the Byrd Station strain network, Antarctica. *J. Glaciol.*, **29**(101), 78–97.

Whillans, I. M. and Y.-H. Tseng. 1995. Automatic tracking of crevasses on satellite images. *Cold Reg. Sci. Technol.*, **23**(2), 201–214.

Whillans, I. M. and C. J. van der Veen. 1993. New and improved determinations of velocity of Ice Streams B and C, West Antarctica. *J. Glaciol.*, **39**(133), 483–490.

## APPENDIX

The regular grid permits the calculation of strain rates by the method described in Nye (1959). For the righthanded coordinate system with axes  $x$  and  $y$ , the strain rates centered at point  $(x_i, y_i)$  are

$$\begin{aligned} \dot{\epsilon}_x &= \frac{1}{4}(b + d - a) + \frac{3}{4}c, \\ \dot{\epsilon}_{xy} &= \frac{1}{2}b - \frac{1}{2}d, \\ \dot{\epsilon}_y &= \frac{3}{4}a + \frac{1}{4}(b + d - c) \end{aligned} \tag{A1}$$

where

$$\begin{aligned} a &= \frac{1}{2}(\ell_{0,1;0,0} + \ell_{0,-1;0,0}) \\ b &= \frac{1}{2}(\ell_{0,1;1,0} + \ell_{0,-1;-1,0}) \\ c &= \frac{1}{2}(\ell_{-1,0;0,0} + \ell_{1,0;0,0}) \\ d &= \frac{1}{2}(\ell_{-1,0;0,1} + \ell_{0,-1;1,0}) \end{aligned} \tag{A2}$$

and

$$\ell_{k,\ell;m,n} = \frac{1}{t} \ln \frac{L_f}{L_i} \tag{A3}$$

is the strain rate along the line between  $(x_{i+k}, y_{j+l})$  and  $(x_{i+m}, y_{j+n})$ , and  $t$  is the time interval over which the line changed from initial length  $L_i$  to final length  $L_f$ . From these equations, the flow-oriented strain rates are

$$\begin{aligned} \dot{\epsilon}_{\text{longitudinal}} &= \dot{\epsilon}_x \cos^2 \alpha + 2\dot{\epsilon}_{xy} \sin \alpha \cos \alpha + \dot{\epsilon}_y \sin^2 \alpha \\ \dot{\epsilon}_{\text{transverse}} &= \dot{\epsilon}_x \sin^2 \alpha - 2\dot{\epsilon}_{xy} \sin \alpha \cos \alpha + \dot{\epsilon}_y \cos^2 \alpha \\ \dot{\epsilon}_{\text{shear}} &= (\dot{\epsilon}_y - \dot{\epsilon}_x) \sin \alpha \cos \alpha + \dot{\epsilon}_{xy} (\cos^2 \alpha - \sin^2 \alpha) \end{aligned}$$

where  $\alpha$  is the flow direction measured counter-clockwise from the  $x$  axis.

MS received 23 November 1995 and accepted in revised form 17 March 1996